International Journal of Advanced Engineering Research and Science (IJAERS)
Peer-Reviewed Journal
ISSN: 2349-6495(P) | 2456-1908(O)
Vol-12, Issue-9; Sep, 2025
Journal Home Page Available: https://ijaers.com/
Article DOI: https://dx.doi.org/10.22161/ijaers.129.1

Optimization Design of Streamline Drag Reduction for Heavy-Duty Buses Based on Fluent

Qi Hong Tang [1], Yan Zuo Chang* [2], Yong Seng Huang[1], Ruo Yu Yang [1], Liu Yi Yu[3], Jian Ting Lai[1], Tian Yi Miao[2], Ying Shan Guo [1]

[1] Department of Energy and Power Engineering, Energy and Power Engineering Major, Guangdong University of Petrochemical Technology, China
[2] Department of Energy and Power Engineering, Guangdong University of Petrochemical Technology, China
[3] Department of Energy and Power Engineering, Process Equipment and Control Engineering major, Guangdong University of Petrochemical Technology, China
*Corresponding author: 17784228714@163.com

Received: 29 Jul 2025,
Received in revised form: 31 Aug 2025,
Accepted: 03 Sep 2025,
Available online: 09 Sep 2025

***Keywords*— large buses, Computational Fluid Dynamics, drag coefficient, external design, Fluent**

***Abstract*—** *In recent years, the global petroleum energy crisis has driven the automotive manufacturing industry to focus on reducing the aerodynamic drag coefficient through optimized design to improve fuel economy, and this demand is particularly prominent in the field of large buses. This paper takes three large buses with different shapes as the research objects, and explores the variation law of their aerodynamic characteristics through streamlined modification of the body shape. In the study, first, a 3lD base model of the large bus was constructed, and three groups of large bus models with different shapes were generated by adjusting the shape parameters. Subsequently, under unified boundary conditions (such as inflow velocity, ambient pressure, etc.), computational fluid dynamics (CFD) methods were adopted, and simulation experiments were carried out with the help of Fluent software. Data such as gas flow field diagrams of each group of models were obtained through numerical simulation, and the influence of different shapes on the aerodynamic drag coefficient was compared and analyzed.The results show that large buses with streamlined designs at the front and rear have better aerodynamic characteristics, and the effect in reducing the drag coefficient is more significant. At the same time, this study can provide a reference basis for the aerodynamic optimization design of large buses.*

I. INTRODUCTION

With the continuous growth of global energy demand, energy structure adjustment and innovation in energy-saving technologies within the transportation sector have emerged as key initiatives to address the energy crisis and environmental challenges. In the transportation field, large buses, as core tools for public transit and long-distance transportation, reducing energy consumption during operation has become a critical issue for alleviating energy pressure and enhancing operational economy. Vehicle energy consumption mainly stems from mechanical losses and aerodynamic drag, with the proportion of these two components dynamically changing with vehicle speed. Among them, aerodynamic drag exerts a particularly significant impact on energy consumption when the vehicle is traveling at high speeds. In aerodynamics, the mechanism by which aerodynamic forces and moments affect vehicle performance and fuel consumption is typically explored through analyzing the distribution of pressure and velocity fields as airflow passes around the vehicle. This provides a theoretical foundation for

reducing the drag coefficient and optimizing energy consumption.

In the early days, traditional large buses relied on wind tunnel experiments to study vehicle aerodynamic characteristics. Early studies pointed out that most large buses, if not adopting streamlined bodies, tend to generate high pressure, thereby leading to significant aerodynamic drag[1]. Krzysztof, K et al. have conducted extensive research on drag reduction for large buses based on computational fluid dynamics (CFD) and wind tunnel experiments, confirming that the drag coefficient can be significantly reduced through measures such as optimizing the streamlined design of the vehicle body, adding flow straightening devices (e.g., fairings, spoilers), adjusting the curvature transition of the front end, and modifying tail structural parameters. Their studies indicated that parameters such as the front side arc, front top arc, and the angle of the tail spoiler have a significant impact on the aerodynamic drag coefficient, and a reasonable combination of these parameters can achieve optimal drag reduction effects[7].In 2011, Wang Xinyu et al. demonstrated that the rational adoption of various aerodynamic drag reduction measures can significantly reduce the wind resistance of buses, effectively achieving energy conservation and consumption reduction[8].In 2012, Liu Quanyou et al. analyzed the relationship between the drag coefficient and vehicle dynamic parameters through simulation using AVL Cruise software. Combined with the formation mechanism of each component of aerodynamic drag, they proposed feasible measures and directions for reducing various resistances [9].In 2015, Sun Qi completed model construction using computer-aided design software Catia and Hypermesh, and conducted simulation analysis of the model utilizing Fluent's powerful computational simulation and post-processing capabilities, thereby carrying out external flow aerodynamic simulation and styling optimization for a passenger car [10].In 2017, Wang Kun attempted to propose different wind resistance optimization schemes for heavy-duty tractor-trailer combinations, and ultimately determined that the optimal wind resistance reduction scheme in the experiment was the wind resistance-optimized tractor combined with a fish-tail trailer [11]. Also in 2017, Ge Jin, Jiang Yuan, and Liu Dongfeng studied and analyzed that vehicle aerodynamic characteristics have a significant impact on vehicle power performance, economy, and stability. Their analysis results showed that the CFD analysis method can effectively meet the requirements of vehicle wind resistance optimization analysis [13].In 2018, Zhao Shiyi and Luo Yili introduced the research on the external aerodynamic performance of various bus bodies using CFD technology, and proposed design methods such as a smoothly curved transition front end, the adoption of front windshield glass with large-radius edges, shortening the Z-direction section of the rain deflector, and keeping the roof structure away from the tail, which improved the flow field around the bus [16].In 2019, Yang Qingcao et al. conducted economic simulation analysis on a light bus using AVL CRUISR software and CFD simulation analysis using STAR-CCM+ software. They proposed a scheme of adding a wind deflector under the bumper, which reduced the overall vehicle drag coefficient by 7.5% compared with traditional methods during bus operation. Additionally, after conducting real-vehicle coasting tests and subsequent simulation analysis on the improved scheme, it was found that fuel consumption decreased by 4.3% when the vehicle speed reached 120 km/h [17].In 2021, Ke Shangji et al. constructed a fuel economy simulation model meeting national standards for a tourist bus using AVL CRUISE, conducted C-WTVC cycle simulation analysis on the model, compared the simulation results with drum test values, analyzed the factors affecting the accuracy of the simulation results, and made corrections [18].In 2023, Li Linlin, based on test data of a light bus meeting National V emission standards, combined parameters of 3 different speed ratio transmissions and 2 different speed ratio rear axle parameters to form 6 powertrains. Using Cruise software, he built a powertrain model for a light bus meeting National VI emission standards and conducted dynamic performance simulation analysis on it [19].

Building on the aforementioned studies, this study aims to explore the correlation laws between the external shape parameters of large buses and the drag coefficient through numerical simulation, establish quantitative relationships between design parameters and driving performance, and provide a theoretical basis and data support for drag optimization in the vehicle design phase.

II. ESTABLISHING THE FLOW FIELD MODEL BASED ON FLUENT

In this study, a 3D base model of a large bus is first constructed. On this basis, three groups of large bus models with distinct morphological characteristics are generated by adjusting the shape parameters. To ensure the consistency and comparability of the research, subsequent experiments are conducted under unified boundary conditions (including parameters such as inflow velocity and ambient pressure). The computational fluid dynamics (CFD) method is adopted, and simulation experiments are carried out with the aid of Fluent software.

2.1. Design concept as mentioned above

The design of this study is based on large buses with approximately rectangular prism-shaped bodies, incorporating smooth and sleek streamlined designs. To gain a more intuitive understanding of the various aerodynamic properties of large buses, simulation and analysis are conducted on their different shape designs, so as to derive the influence of different shape designs on the variation of the drag coefficient of large buses [22]. The geometric shapes of the three different external designs of large buses designed in this study are shown in Figure 1.

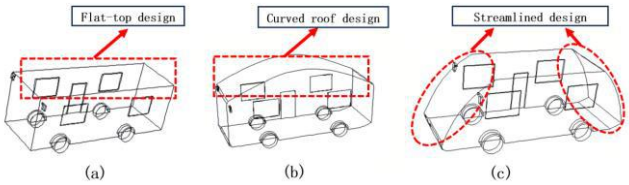

Fig. 1: Design drawings of three large buses with different external designs

The above are the conceptual diagrams of the geometric designs for three large buses with different external shapes. As can be seen from the diagrams, Fig. 1(b) differs from Fig. 1(a) in the shape of the roof: the roof of Fig. 1(a) is designed as a flat roof, while that of Fig. 1(b) is designed as a convex curved roof. In comparison, Fig. 1(c) differs from Fig. 1(a) in the shapes of the front and rear ends: Fig. 1(a) is designed with flat front and rear ends, whereas Fig.1(c) features smooth front and rear ends, which are more in line with streamlined design. The following is the data table of basic dimensions for each large bus.

Table. 1: Dimension Data Sheet

	Design 1	Design 2	Design 3
Vehicle Body Length (m)	12.0	12.0	12.0
Vehicle Body Width (m)	4 . 0	4.0	4.0
Vehicle Body Height (m)	4.0	6.0	4.0
Front Track (m)	3.6	3.6	3.6
Rear Track (m)	2.4	2.4	2.4
Front Overhang (m)	3.6	3.6	3.6
Wheelbase (m)	6.0	6.0	6.0
Tire Radius (m)	0.4	0.4	0.4
Tire Width (m)	0.4	0.4	0.4
Weight (kg)	12200	12200	12200
Approach Angle (°)	9	9	9
Departure Angle (°)	8	8	8

In reality, the aerodynamic behavior of large buses during operation is generally asymmetric. However, considering the computational capacity of computers, it is necessary to appropriately simplify the problem. Therefore, the bus model is depicted in a symmetric manner and simplified into a relatively simple geometric shape for computational analysis. The process of fluid computation can be simplified into the following flow chart.

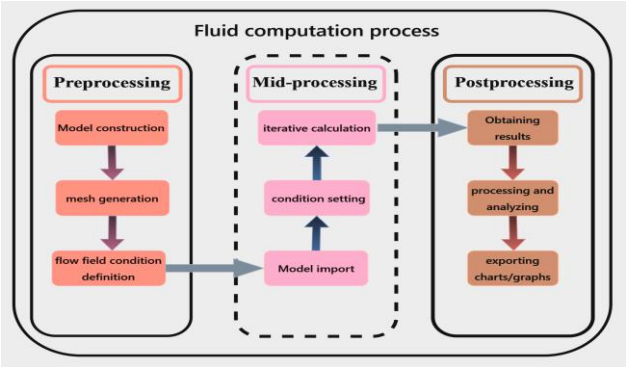

Fig. 2: Fluid computation process

2.2. Mesh Generation

Prior to conducting simulation analyses in this study, grid nodes must first be constructed according to the external geometry of the built large bus geometric models. For the physical models of large buses with different geometric shapes, to achieve better mesh quality, this study adopts a multi-block structured mesh system. Within the computational domain, the mesh is divided into uniform and non-uniform mesh systems to improve computational accuracy. Mesh generation for the physical models of each large bus and their computational domains was performed using Fluent, and the schematic diagram of the grid node system in the computational domain is shown in Fig. 3.

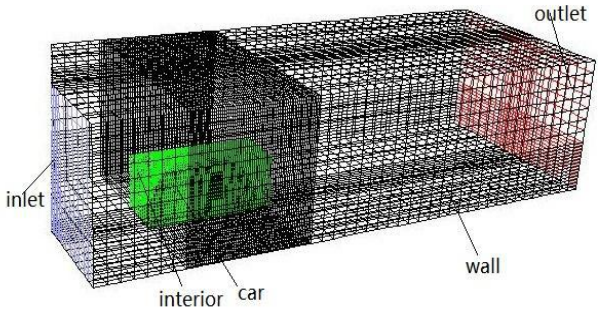

Fig.3: Schematic Diagram of the Full Computational Domain Mesh

For numerical simulation of flow field problems, the computational domain must be defined as a finite domain, which is typically composed of multiple overlapping mesh blocks, with the overlapping regions of the blocks regarded as boundaries [23]. The setting of boundary conditions directly affects the accuracy of flow field calculations and is closely related to boundary grid nodes and inter-mesh flux calculations. Therefore, flow field calculation programs need to be equipped with mesh recognition functions to process grid nodes **Error! Reference source not found.**.For the present study, boundary conditions must be set in accordance with the actual operating conditions of large buses. Their rationality is critical to ensuring the accuracy of analyzing aerodynamic characteristics (including pressure contours, local pressure variations, streamline patterns, and drag coefficients). Hence, rigorous configuration is required.

To facilitate comparison of the flow field characteristics among buses with different external shapes, uniform boundary conditions are applied to all physical models. The flow field inlet is set as a free-stream velocity inlet with a constant speed of 72 km/h, simulating airflow directed toward an infinite space. The outlet is configured as a pressure outlet, mimicking airflow discharge into the ambient atmosphere. The wall surfaces of the bus bodies satisfy the conditions of impermeability and no-slip. The interior boundary of each bus is defined as "interior," while the external environment boundary adopts the default settings of the Fluent system.

2.3. Calculation formulas for flow field analysis

（1）turbulence model

In the current research stage, turbulence models in turbulence model theory can be categorized into several types based on the number of equations, including two-equation models, one-equation models, seven-equation models, and zero-equation models (algebraic models), etc. [22]. Meanwhile, commonly used models in Fluent include the k-ε model, Reynolds Stress Model (RSM), Algebraic Stress Model (ASM), etc. Among them, although RSM achieves high computational accuracy, it requires solving seven partial differential equations, which leads to a complex process, large computational load, and high demands on computer performance, thus limiting its wide practical application. As a simplified version of RSM, ASM reduces computational time and does not sacrifice accuracy in some analyses; however, it has greater limitations and is also not widely applied. Compared with the aforementioned two models, the k-ε model only needs to solve two equations, resulting in a relatively small computational load. Moreover, it has good adaptability to flow around bluff bodies (such as external flow fields around vehicles), can accurately capture pressure distribution and drag characteristics, and exhibits strong parameter robustness. Therefore, after comparative analysis in the study, the k-ε model is adopted in this experiment.

In the k-ε turbulence model, k refers to turbulent kinetic energy, and ε refers to turbulent dissipation rate, which are two crucial parameters in the k-ε turbulence model. CFD simulations of turbulent flow fields generally adopt the Standard k-ε turbulence model. The RNG k-ε turbulence model, based on the standard model, exhibits better performance in handling industrial boundary effects in numerical simulations, with more accurate calculation results. Therefore, the RNG k-ε turbulence model is adopted in this study.

The RNG k-ε turbulence model is similar to the Standard k-ε turbulence model, but it incorporates an additional condition into the dissipation rate equation, accounting for turbulent vortices, which has achieved effective improvements in terms of accuracy. These characteristics enable the RNG k-ε turbulence model to exhibit higher reliability and accuracy in a wider range of flows compared to the Standard k-ε model **Error! Reference source not found.**. Equations 1 and 2 are the transport equations for turbulent kinetic energy k and turbulent dissipation rate ε, respectively, as follows:

$$\frac{\partial(\rho k)}{\partial t}+\frac{\partial}{\partial x_i}(\rho k U)=\frac{\partial}{\partial x_i}\left(\alpha_k \mu_{eff}\frac{\partial k}{\partial x_i}\right)+G_k-\rho\varepsilon \quad (1)$$

$$\frac{\partial(\rho\varepsilon)}{\partial t}+\frac{\partial}{\partial x_i}(\rho\varepsilon U)==\frac{\partial}{\partial x_i}\left(\alpha_\varepsilon \mu_{eff}\frac{\partial \varepsilon}{\partial x_i}\right)-C_{1\varepsilon}\frac{\varepsilon}{k}(G_k)-C'_{2\varepsilon}\rho\frac{\varepsilon^2}{k} \quad (2)$$

$$C'_{2\varepsilon}=C_{2\varepsilon}+\frac{C_\mu\eta^3\left(1-\frac{\eta}{\eta_0}\right)}{1+\beta\eta^3} \quad (3)$$

$$\eta=\frac{Sk}{\varepsilon} \quad (4)$$

In the above equations, the parameters are as follows: C1ε=1.42， C2ε=1.68， η0=4.38， β=0.012. Both αk andαε are inverses of the Prandtl numbers. Under conditions of high-Reynolds-number flow fields,

αk=αε≈1.939. The coefficients of the transport equations for the RNG k-ε turbulence model are basically the same as those for the Standard k-ε turbulence model.

（2）. Numerical simulation

In Fluent, the conversion of governing equations and geometric algebraic equations is typically performed based on the control volume method, which is then solved using appropriate numerical approaches. The control volume method involves integrating the discretized governing equations for each control volume, ensuring that the discretized control volume governing equations achieve the steady-state conservation of physical quantities [22].This study considers the equation for maintaining the steady-state conservation of a physical quantity ϕ, whose governing equation can be expressed in terms of the control volume as follows, where V denotes the control volume.

$$\oint \rho\phi\vec{u}\cdot d\vec{A} = \oint \Gamma_\phi \nabla\phi \cdot d\vec{A} + \int S_\phi dV \tag{5}$$

$$\sum_{f}^{N_{face}} \rho_f \vec{u_f}\phi_f \cdot \vec{A_f} = \sum_{f}^{N_{face}} \Gamma_\phi (\nabla\phi)_n \cdot \vec{A_f} + S_{\phi v} \tag{6}$$

Equation 6 is derived by discretizing Equation 5. Here, $\vec{u}$ represents the velocity vector, $\vec{A}$ denotes the surface area vector, Γ_ϕ is the diffusion coefficient, S_ϕ is the source term per unit control volume, N_{face} is the number of control volume faces, ϕ_f is the value of ϕ passing through the control volume face f, and $\overrightarrow{A_f}$ is the surface area vector of the control volume face f.

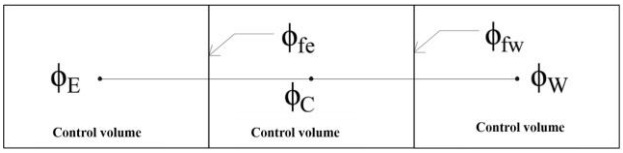

Fig. 4: Control Volume and Discretization

The discretized values of ϕ are stored within the control volume, as shown in Fig. 2.1 below, such as ϕE (East), ϕW (West), and ϕC (Center), etc. However, the values of ϕ between faces within the control volume are actually unknown; at this point, it is necessary to obtain interpolated solutions using the values of ϕ[23]. In practical applications, the direction of fluid motion needs to be considered as the directional guidance for deriving these interpolated solutions, thus leading to the use of the upwind scheme, which handles discretization based on convective terms. This engineering design employs the first-order upwind scheme for initial iterative calculations to ensure numerical stability.

III. ANALYSIS OF SIMULATION RESULTS

The first paragraph under each heading or subheading should be flush left, and subsequent paragraphs should have a five-space indentation. A colon is inserted before an equation is presented, but there is no punctuation following the equation. All equations are numbered and referred to in the text solely by a number enclosed in a round bracket (i.e., (3) reads as "equation 3"). Ensure that any miscellaneous numbering system you use in your paper cannot be confused with a reference [4] or an equation (3) designation.

To investigate the impact of different external designs on the airflow characteristics of large buses during operation, the following analysis will conduct a detailed examination of three large buses with distinct external designs, focusing on aspects such as pressure distribution on the vehicle body, airflow velocity distribution, surrounding flow field, flow separation, and wake region.

3.1. Pressure Analysis of Large Bus Bodies

When a large bus is in motion, airflow impinging on the front of the bus flows along the body, eventually directed toward the infinite space behind the bus. Due to differences in geometric shapes among various body parts of buses with different external designs, the behavior of airflow passing over the body varies to some extent across different sections. The aerodynamic forces acting on a large bus are related to its surrounding pressure distribution, which in turn depends on the streamline characteristics of the body. The following are diagrams illustrating the body pressure distribution of three large buses with different external designs during operation.

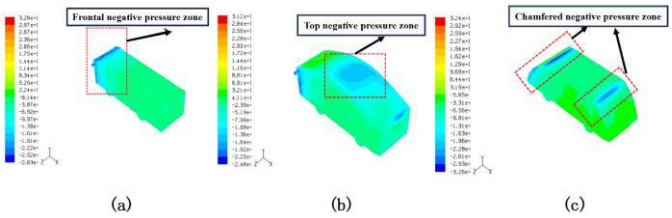

Fig. 5: Contour Map of Pressure Distribution on the Large Bus Body

The pressure distribution in Fig.5(a) shows that the airflow is significantly obstructed when flowing over the front of the bus. According to Bernoulli's equation, as the velocity decreases, the pressure gradually increases. Due to the absence of chamfers, local separation of airflow occurs at the corner of the front, forming a negative pressure zone. The pressure on the bus body gradually recovers from the maximum negative pressure at the front and tends to stabilize. Moreover, along the direction of the bus body, the maximum pressure remains negative, and the

entire bus body, except for the front, is basically in a state of negative pressure.

Design 2 differs from Design 1 in streamline design. As shown in Fig.5(b), its front pressure is higher, indicating more severe airflow obstruction and lower velocity. Due to the chamfer design on the upper part of the front, there is less airflow separation and no negative pressure zone. The pressure on the upper part of the body first decreases then increases, and becomes basically negative after the middle section. The pressure on the left and right sides gradually increases along the body and shows a distribution of lower at the top and higher at the bottom. Overall, the pressure is higher than that of Design 1.

The streamline design of Design 3, as shown in Fig.5(c), results in lower front pressure, indicating less airflow obstruction and higher velocity. Due to insufficient streamline smoothness of the guide angle on the upper part of the front, airflow separation is severe, forming a negative pressure zone. The pressure on the vehicle body recovers from the maximum negative pressure at the front, reaches the highest point in the upper middle section, and then decreases. The pressure on the left and right sides recovers from the lowest point at the front and then stabilizes. Along the direction of the vehicle body, the maximum pressure remains negative, and the overall pressure is higher than that of Design 1.

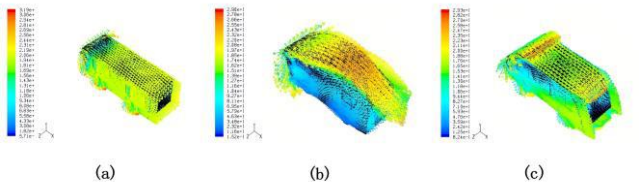

Fig. 6: Velocity Vector Diagram of the Large Bus

The velocity vector diagram of Design 1, as shown in Fig.6(a), indicates that the oncoming airflow splits into three parts upon encountering the front of the vehicle, flowing respectively over the windshield, above and below the front, and along the side of the vehicle towards the rear. Due to the truncated tail design of the vehicle, the airflow fails to adhere closely to the vehicle body, forming a low-velocity vortex region behind the vehicle.

Design 2 differs from Design 1 in streamline configuration. As shown in Fig.6(b), the overall airflow velocity at the front is lower, indicating more severe airflow obstruction. Due to the chamfer design on the upper part of the front, there is less airflow separation, and the velocity variation is gentler compared to Design 1. Affected by the convex design of the roof, the airflow velocity on the upper part of the vehicle body first increases then decreases, reaching the highest point at the middle section. The airflow velocity on the left and right sides of the vehicle body shows little variation along the body, and the overall velocity is lower than that of Design 1.

Design 3 differs from Design 1 in streamline configuration. As shown in Fig.6(c), the airflow velocity at its front is higher, with less severe airflow obstruction. Due to insufficient streamline smoothness of the chamfer on the upper part of the front, airflow separation is more severe, forming a negative pressure zone, and the magnitude of velocity variation is similar to that of Design 1. The airflow velocity on the upper part of the vehicle body decreases from the highest point at the front, then remains stable, and increases when passing through the streamlined tail. The airflow velocity on the left and right sides of the vehicle body gradually increases from the lowest point at the front, reaching the highest point at the rear of the vehicle. Overall, the velocity is lower than that of Design 1.

The body-related data of large buses with three different external designs are shown in the following table.

Table. 2: Vehicle Body Surface Data

	Design 1	Design 2	Design 3
Maximum Pressure (pascal)	182.2	272.32	152.18
Minimum Pressure (pascal)	-560.7	-518.8	-444.58
Total Pressure (pascal)	-1112494.6	-129762.25	-895442.13
Average Pressure (Pascal)	-60.87	-7.55	-49.43
Maximum Velocity (m/s)	31.04	24.98	26.18
Minimum Velocity (m/s)	0.57	0.002	0.24
Average Velocity (m/s)	16.92	4.58	10.47

From the above table, it can be concluded that the overall average body pressure of the various large buses follows the order: Design 1 < Design 3 < Design 2, while the average velocity follows the order: Design 1 > Design 3 > Design 2. The magnitudes of the body pressure and airflow velocity of a large bus during operation are related to a certain extent to its drag coefficient. Since flow separation leads to significant energy loss, the design in this study should strive to prevent flow separation or reduce the vortex action area. Among the aforementioned large buses, Design 2 and Design 3, due to their chamfer configurations, have reduced flow separation to a certain

extent, which has a positive effect on improving pressure drag and thereby reducing the drag coefficient of large buses.

3.2. Analysis of the Surrounding Flow Field of Large Buses

When a large bus is in motion, in addition to the data and diagrams related to the bus body itself, research and analysis of the surrounding flow field are also essential. During operation, a large bus will disturb the original motion trajectory, velocity, and pressure of the surrounding airflow. The following are cross-sectional diagrams of the surrounding pressure for three large buses with different external designs:

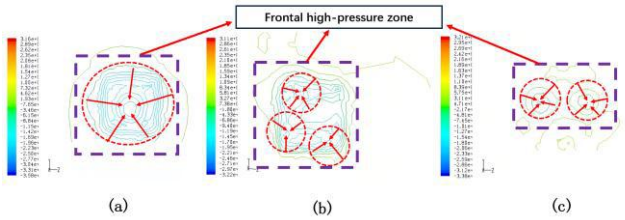

Fig. 7: Cross-sectional Diagram of Pressure around the Large Bus

From the contour maps of pressure distribution on the surrounding cross-sections of the buses with three different designs in Fig. 7, it can be observed that when the airflow flows over the surface of the large bus body, the oncoming airflow first encounters the front part of the vehicle. Here, the airflow is obstructed, resulting in a significant reduction in velocity and a substantial increase in pressure. Consequently, the dynamic pressure of the airflow is converted into static pressure, forming one or more high-pressure zones in front of the vehicle head. In addition, the flow fields near other parts of the vehicle body also exhibit certain variations. Calculated using Fluent software, the flow field-related data of large buses with different external designs are shown in the following table.

Table. 3: Flow Field Pressure Data

	Design 1	Design 2	Design 3
Maximum Pressure (pascal)	315.56	311.46	321.4
Minimum Pressure (pascal)	-560.75	-518.8	-444.58
Total Pressure (pascal)	-14990774.01	-408238.1	-10476264.02
Average Pressure (Pascal)	-1.85	16.17	3.07
Maximum Velocity (m/s)	31.88	29.95	29.33
Minimum Velocity (m/s)	0.57	0.02	0.08
Total Velocity (m/s)	5951018	2261026	4595286
Average Velocity (m/s)	20.15	19.8	20.16

From the above table, it can be concluded that the overall average pressure of the flow field for various large buses follows the order: Design 1 < Design 3 < Design 2, while the overall average velocity of the flow field follows the order: Design 2 < Design 1 < Design 3. However, the average pressure and velocity of the flow fields for buses with different external designs show little difference.

3.2.1. flow separation

Flow separation is the core factor leading to increased aerodynamic drag. The negative pressure field formed in the vehicle body's vortex zone and the positive pressure region at the front of the vehicle form a significant pressure gradient, thereby generating pressure drag. According to Bernoulli's principle, an increase in pressure in a fluid system is accompanied by a decrease in kinetic energy, causing the airflow in the boundary layer affected by viscous forces to struggle to continue advancing in the flow direction within the high-pressure region due to insufficient kinetic energy [24]. Meanwhile, driven by the pressure gradient, reverse flow occurs in the fluid near the wall, eventually resulting in separation from the wall. The separation point is defined as the boundary between downstream and upstream flows in the outermost layer of the wall, where the wall-normal pressure gradient is zero and the wall shear stress vanishes. The probability of flow separation is positively correlated with the pressure rise slope: the steeper the pressure rise slope, the higher the risk of separation.

Flow separation induces significant energy dissipation; thus, one of the core objectives of this study is to suppress flow separation or reduce the vortex-affected area. Comparative analysis indicates that the Case2 and Case3 vehicle models have effectively reduced the degree of flow separation through their chamfer designs, which exert a positive effect on optimizing pressure drag and reducing the drag coefficient. Due to geometric constraints, airflow on the surface of large buses is prone to early separation, and large-scale turbulence tends to form in the rear area of the vehicle, resulting in a significant increase in pressure drag.

3.3. Analysis of the Wake Region of Large Buses

The wake refers to the turbulent vortex flow behind or downstream of a moving object. When airflow flows around a large bus, a very thin boundary layer vortex region forms on the surface adjacent to the bus. The airflow separates from the rear surface of the bus, and vortices detach intermittently from the rear surface of the bus. These thin boundary layers and the separated airflow

vortex regions flow downstream, forming a turbulent wake filled with various vortices at the rear of the bus [25]. The following is an analysis of the wake research on large buses with different external designs.

To investigate, analyze, and compare the flow characteristics of the fluid near the rear of the bus body during the operation of large buses, this engineering design has captured the rear streamline diagrams and planar diagrams of rear streamline velocity for three large buses with different external designs in motion. The wake cross-sections are uniformly set as the cross-sections perpendicular to the ground, 0.5 meters from the rear surface of the bus body, as shown in Fig. 8.

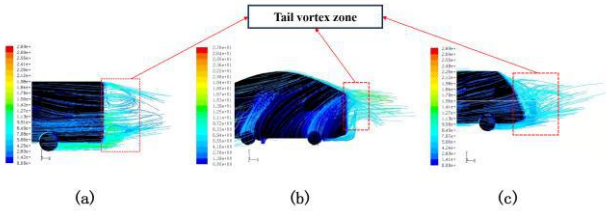

Fig. 8: Streamline Diagram of the Large Bus Rear

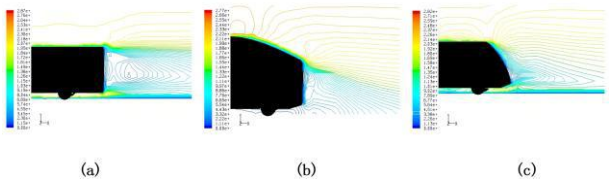

Fig. 9: Plan View of Wake Velocity for Large Bus

Through comparative analysis of the rear streamline diagrams and streamline diagrams of rear cross-sections of three large buses with different external designs during operation as shown in Figs. 8 and 9, it can be concluded that:

As shown in Fig.8(a), the rear streamlines of Design 1 indicate that the airflow flows along the surface from the middle part to the rear of the vehicle body. Due to the truncated tail design of the vehicle rear, the airflow fails to adhere closely to the vehicle body, leading to local separation behind the vehicle and forming two negative pressure vortex zones, with a significant reduction in velocity. Additionally, there are two negative pressure peaks in the vortex zones, and the streamlines converge behind the vehicle. The area of its vortex zones is shown in Fig.9(a).

As shown in Fig.8(b), the rear streamlines of Design 2 indicate that the airflow flows along the surface from the middle part to the rear of the vehicle body. Due to the special convex design of the roof with chamfers formed, there is less airflow separation above the front of the vehicle, and more airflow adheres closely to the rear surface of the vehicle body compared to Design 1; thus, the formed vortex action area is smaller than that of Design 1. However, the airflow below the vehicle body still forms partial vortices due to the influence of chamfers. The streamlines converge behind the vehicle, with relatively large differences in airflow velocity and pressure, and the flow is more complex than that of Design 1. The vortex area in its wake region is smaller than that of Design 1, as shown in Fig.9(b).

As shown in Fig.8(c), the rear streamlines of Design 3 indicate that the airflow flows along the surface from the middle part to the rear of the vehicle body. Due to the special curved surface design at the rear of the vehicle, there is less airflow separation above the front of the vehicle, and more airflow adheres closely to the rear surface of the vehicle body compared to Design 1, resulting in a vortex action area smaller than that of Design 1. The airflow below the vehicle body still forms partial vortices due to the influence of chamfers; the streamlines converge behind the vehicle, with relatively large differences in airflow velocity and pressure, and the motion trajectories and pressure changes are more complex. The vortex area in its wake region is smaller than that of Design 1. Similar to Design 2, the curved surface transition further delays the separation point on the upper surface, expanding the attached flow region; the airflow at the bottom is also affected by the upward lift of the curved surface, forming a weaker double-vortex structure. The total area of the trailing vortices is significantly reduced compared to Design 1, but the interaction between vortex systems is enhanced, leading to an increase in local turbulent kinetic energy, as shown in Fig.9(c).

Calculated using Fluent 6.3.26 software, the relevant data of the wake flow field cross-sections for large buses with different external designs are shown in the following table.

Table. 4: Data Sheet of Cross-sections of Wake Flow Field

	Design 1	Design 2	Design 3
Maximum Velocity (m/s)	29.36	29.47	29.77
Minimum Velocity (m/s)	1.67	0.25	0.63
Average Velocity (m/s)	14.09	13.4	13.31
Maximum Pressure (pascal)	-4.77	24.2	27.23
Minimum Pressure (pascal)	-178.47	-202.45	-47.8
Average Pressure (Pascal)	-53.83	-19.86	0.08

From the above table, it can be concluded that during the operation of the large buses designed in this study, the wakes formed by the three models with different external designs exhibit differences. Among them, Design 2 shows the largest variations in wake cross-sectional pressure and velocity, followed by Design 1, and then Design 3. In terms of overall averages, the order is Design 1 < Design 2 < Design 3. This indicates that the external design has a significant impact on the operation of large buses. Designing the external shape of large buses to be streamlined exerts a certain influence on both the vehicle body surface and the nearby flow field. Due to differences in streamline treatments among the buses, the distribution of differences in cross-sectional pressure of the wake surface also varies; in particular, the larger the streamline area, the more pronounced the variation.

IV. CONCLUSION

Combining the previous simulation research and analysis, and using Fluent software for calculations, the drag coefficients and related data of the large buses in this engineering design are as follows:

Table. 5: Data Comparison Table

	Design 1	Design2	Design 3
Pressure Coefficient of Frontal Windward Surface of Vehicle Head (Cp)	0.63	0.5	0.39
Drag Coefficient (Cd)	0.69	0.51	0.43
Percentage of Aerodynamic Drag Coefficient Reduction (△Cd) (%)	0	26.1	37.7

Based on the simulation results in the table combined with the simulation analysis within the design of this study, the conclusions of this study can be drawn as follows:

This study focuses on the aerodynamic characteristics of large buses, aiming to reduce the drag coefficient and improve driving performance through streamlined designs. Numerical simulation results indicate that streamlined designs have a significant effect on drag reduction: Design 2, which only adopts a curved design for the roof, can reduce wind resistance to a certain extent but with limited effectiveness; in contrast, Design 3, which implements streamlined designs for both the front and rear of the vehicle, can significantly reduce pressure drag by increasing the pressure at the rear of the vehicle and reducing the vortex action area, exhibiting the most prominent drag reduction effect. Therefore, Design 3 is identified as the optimal scheme. Meanwhile, this design predicts the aerodynamic characteristics and their impact on driving conditions in advance during the bus development stage. By optimizing the external design, it effectively reduces the drag coefficient, enhances driving performance, and simultaneously takes into account the aesthetic value of the design. In summary, through the integration of streamlined design and numerical simulation, this study has clarified the optimal external design scheme for large buses, providing a reference for the optimization of aerodynamic characteristics of similar vehicle models.

In addition, although this engineering design has studied and analyzed the aerodynamic characteristics of large buses with different external shapes during operation and compared the relevant design results, the study has certain limitations. Future research can be extended to conduct more comprehensive studies and analyses through the following approaches: generating higher-quality meshes for the large bus model and computational domain, increasing the number of iteration steps to improve computational precision and result accuracy; performing numerical simulations under different driving speeds and analyzing relevant graph data to investigate the impacts on driving performance and aerodynamic characteristics, thereby obtaining more accurate and comprehensive data; and further optimizing the design to address existing issues such as insufficient computer performance, so as to achieve better results.

ACKNOWLEDGEMENTS

This work described in this paper was supported by The Research Funding of GDUPT, Research on Lagrangian Coherent Structure Analysis of Heat Sink for Heat Transfer Performance with Piezoelectric Fan. Guangdong Science and Technology Program in 2024, (Project No.: 2024A0505050022). Research on Intelligent Monitoring and Control Technology of Air Conditioning Noise Based on Quantitative Conjugate Gradient Method. Guangdong College Students' Innovation and Entrepreneurship Program in 2025, (Project No.: 25A015).

REFERENCES

[1] Aikpo, F. H., Ahouanse, M. D., Agbandji, L., Edorh, P. A., & Houssou, C. S. (2017). Assessment of contamination of soil by pesticides in Djidja's cotton area in Benin. *International Journal of Advanced Engineering Research and Science, 4*(7), 1-5. doi:10.22161/ijaers.4.7.1

[2] Questia. (n.d.). Retrieved November 20, 2022, from http://www.questia.com/read/107598848

[3] Halyut, H. I., & Abed, P. D. (2022). A critical stylistic analysis of the representation of the Iraqi local society in Sinan Antoon's The Corpse Washer. *International Journal of English Literature and Social Sciences, 7*(6), 001-010. doi:10.22161/ijels.76.1

[4] Philip, E., & Philip, A. (2022). The influence of positive self-affirmation towards Malaysian ESL students at tertiary level of Education. *Journal of Humanities and Education Development, 4*(4), 09-17. doi:10.22161/jhed.4.4.2

[5] Ifeanyi, I. C. (2022). Micronutrient concentrations of cassava continuously cultivated soils in Ezinihitte Mbaise LGA Imo State, Nigeria. *International Journal of Environment, Agriculture and Biotechnology, 7*(5), 001-007. doi:10.22161/ijeab.75.1

[6] LIU, J. S., XU, S. J., WANG, Q. Y., BAO, H. H., & WANG, Y. (2020). Review of automotive aerodynamics research based on physical models. *Journal of Experiments in Fluid Mechanics*, 34(1), 38-48.

[7] Krzysztof, K., Michal, R., & Janusz, P. (2019) The Influence of Different Aerodynamic Setups on Enhancing a Sports Car's Braking. *International Journal of Mechanical Sciences*, 164

[8] WANG, X. Y. WANG, D. F., FAN, S. J., &FU, Q. (2011). Research and application of aerodynamic drag reduction devices on commercial vehicle. *Journal of Mechanical Engineering*, 47(6), 107-112.

[9] LIU, Q. Y., ZHAO, F. Q., YANG, A. Z., JIN, J. G., & ZHAI, H. J. (2012). Analysis of automobile drag coefficient. *Agricultural Equipment & Vehicle Engineering*, 50(11), 59-62.

[10] SUN, Q. (2015). *Numerical simulation and model optimization for car body (Master's thesis)*. Shanghai University of Engineering Science.

[11] WANG, K. (2017). *Analysis and verification of aerodynamic drag optimization for heavy-duty tractor-trailers* (Master's thesis). Jiangsu University.

[12] K. Salari, j. Ortega, p.Castellucci. Computational prediction of aerodynamic forces for a simplified intergrated tractor-trailer geometry[J].*Journal of Food Science.*2013, 55(55):1172-1173.

[13] GE, J., JIANG, Y., & LIU, D. F. (2017). Based on CFD analysis of a tractor wind resistance coefficient optimization. *Automobile Applied Technology*, 14, 118-120.

[14] TONG, H. H. (2018). Patent design of reducing coach wind resistance from pressure difference. *Bus Technology and Research*, 40(1), 34-35.

[15] HE, H. R., SUN, Q. Y., & LU, F. L. (2018). Influence of rear spoiler on vehicle aerodynamic drag. *Agricultural Equipment & Vehicle Engineering*, 56(2), 33-36.

[16] ZHAO, S. Y., & LUO, Y. L. (2018). CFD study on aerodynamic performance outside bus body. *Bus Technology*, 4, 9-12.

[17] YANG, Q. C., FANG, D. G., LI, Z. J., ZHU, X., & YUAN, L. K. (2019). Optimization of drag coefficient based on reducing fuel consumption. *Light Vehicle Technology*, (Z3), 16-19+28.

[18] KE, S. J., & QIAN, X. D. (2021). Simulation analysis and verification of bus economy based on AVL CRUISE. *Bus Technology and Research*, 43(2), 32-34.https://doi.org/10.15917/j.cnki.1006-3331.2021.02.011

[19] LI, L. L. (2023). Simulation analysis of dynamic and economy for light passenger meeting China-VI vehicle emission standard. *Diesel Engine Design and Manufacture,* 29(2), 19-22.

[20] LIU, C. (2015). *A dissertation in power engineering and engineering thermophysics* (Master's thesis). Anhui University of Science and Technology.

[21] Andreas Borg， Sven Perzon， Olga Roditcheva. On the influence of the near wall formulation of the turbulence models for prediction of aerodynamic coefficients for ground vehicles. *SAE technique paper*,2003-01-1317.

[22] ZHOU, X. (2016). *Research on low aerodynamic drag design and aerodynamic optimization of a certain vehicle model* (Master's thesis). Jilin University.

[23] LI, J. L. (2009). *Numerical simulation research on flow field of chain-driven wind energy conversion device* (Master's thesis). Inner Mongolia University of Technology.

[24] QU, P., & LIU, X. Y. (2020). A virtual analysis method for automobile wind noise and wind resistance. *Auto Engineer*, (), 56-57.

[25] F. H., R., D., S., & C., B. (2020) Unsteady Aerodynamic Forces on Long Lorry Platoons, *Journal of Wind Engineering and Industrial Aerodynamics*, 209: 104481-104481.